Journal of Energy Storage 73 (2023) 109147

Contents lists available at ScienceDirect

Journal of Energy Storage

journal homepage: www.elsevier.com/locate/est

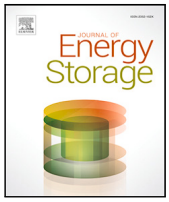

Research papers

A continuous multiphase model for liquid metal batteries

Omar E. Godinez-Brizuela [a,*], Carolina Duczek [b], Norbert Weber [b], William Nash [b], Martins Sarma [b], Kristian E. Einarsrud [a]

[a] Norwegian University of Science and Technology, Trondheim, 7030, Norway
[b] Helmholtz Zentrum Dresden-Rosendorf, Bautzner Landstr. 400, Dresden, 01328, Germany

ARTICLE INFO

Keywords:
Liquid metal battery
Energy storage
Multiphase flow
Na-Zn

ABSTRACT

Liquid metal batteries (LMBs) are a promising candidate for large-scale stationary storage of renewably generated energy. Their Earth-abundant electrode materials and highly conductive molten salt electrolytes confer the low costs and high power densities required for grid-scale storage. LMB operation involves a complex interplay between mass transport mechanisms, and as a result their performance potential and operational limits are not fully understood. In this study, a multiphase numerical model is presented that simulates the charge and discharge processes of an LMB based on the Na-Zn couple. The model computes the changes in electrode and electrolyte volume, and resolves the spatial variations in the chemistry of the electrolyte that accompany the interfacial reactions. Volume change and species redistribution were found to be important in predicting the maximum theoretical capacity of the cell when neglecting other transport mechanisms.

1. Introduction

The transition to clean energy sources presents a number of unsolved technological challenges. In recent years, it has become clear that a significant reconfiguration of the technologies used for energy production and distribution will become necessary [1–3]. Many renewable energy sources are intermittent in nature; they are only available at certain times of the day and when certain conditions are met, leading to frequent imbalances between supply and demand. Stationary, large-scale energy storage is necessary for the proliferation of renewables, but the existing technologies have significant limitations that make them suboptimal for applications that require high capacity and flexibility. Liquid Metal Batteries (LMBs) have emerged as a promising solution to many of the challenges in energy supply, offering high capacity and reliability [4], despite being produced from abundant and low-cost materials. This technology has emerged as an alternative to other grid-level technologies available, such as pumped-hydro or large stacks of Li-ion batteries, since it addresses some of the disadvantages that make these systems infeasible, such as fire-related risks and high costs in the case of Li-ion [5,6], or geographic infeasibility as in the case of pumped-hydro.

In general, LMBs consist of a pair of molten metal electrodes separated by a molten salt electrolyte: usually a eutectic mixture of metal halides. These phases form a stable three-layered metal-salt-metal structure due to their large contrasts in density [7,8], and the immiscibility between the metals and the salt. During discharge of an LMB, energy is liberated by coupled metal–metal halide reactions occurring at the two electrode-electrolyte interfaces. Successful LMB design entails the selection of metals and salts for which these coupled reactions yield the highest voltage for the lowest material cost. Machine learning algorithms have even been enlisted for this purpose [9], and a large range of cell chemistries have been experimentally investigated, such as Li-Bi, Pb-Sb and Ca-Bi [10–12]. One of the most recently investigated chemistries is Na-Zn [13–15], which exhibits an unusually high theoretical voltage of 1.87 V [16], and is the subject of this paper.

The primary motivation for developing Na-Zn cell is the attractive cost of its electrode materials, as these are low even by the standards of LMBs. In general, LMB anodes must exhibit low-densities and low melting temperatures, and thus Li has historically been a popular candidate [10,17]. However lithium is expensive and not always readily available. Other alternatives include gallium [18] or sodium-potassium alloys [19,20], but these are not easily scaled to massive storage applications due to cost and safety concerns [20,21]. Na combines manageable safety levels with low cost. As LMB cathodes, suitable materials are sometimes prohibitively expensive, of low abundance [22], or have other unfavorable properties, such as promoting corrosion and other forms of cell degradation [5]. This leads to limited favorable options, but among these, Zn is particularly attractive due to its low cost and safety advantages [17].

In addition, electrolyte components that are compatible with the Na-Zn cell are cheap and readily available, namely NaCl, $ZnCl_2$ and

* Corresponding author.
E-mail address: omar.godinez@sintef.no (O.E. Godinez-Brizuela).

https://doi.org/10.1016/j.est.2023.109147
Received 12 April 2023; Received in revised form 15 August 2023; Accepted 29 September 2023
Available online 9 October 2023

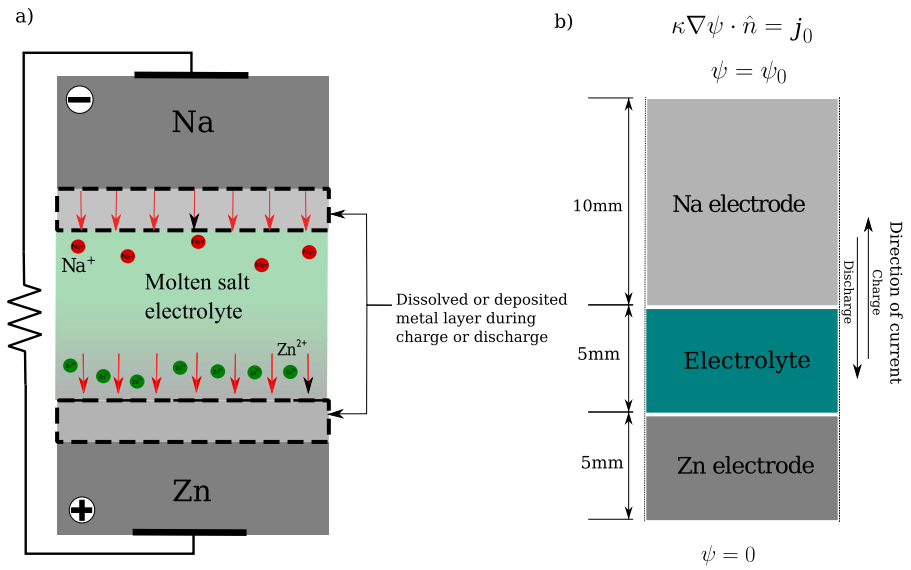

Fig. 1. Schematic figure of the Na-Zn liquid metal battery, showing the range of positions for the electrode-electrolyte interfaces (black dashed lines) and the direction of the flux in red arrows during discharge (a). Schematic showing the dimensions of the model domain and potential boundary conditions (b). (For interpretation of the references to color in this figure legend, the reader is referred to the web version of this article.)

others [23,24]. Addition for example of iodides can significantly reduce the melting point, but comes with increased cost [5]. The melting point of the electrolyte must be compatible with the operating temperature of the electrodes and should exhibit a high ionic conductivity with a low electronic conductivity [2,5,25–27].

A schematic of the Na-Zn cell is shown in Fig. 1. During discharge, Na from the negative electrode is oxidized and dissolves in the salt as Na^+ ions, displacing the Zn^2+ ions that are simultaneously reduced and deposited into the positive electrode as Zn metal. This process is reversed during the charging process. The salt electrolyte contains NaCl, $ZnCl_2$ – which participate in the interfacial reactions – and $CaCl_2$, which functions as a spectator but is included to lower the melting point of the salt.

It should be noted that the Na-Zn cell differs from most previous LMB designs regarding the nature and co-ordination of its coupled interfactial reactions. During discharge, Na displaces Zn in the salt, and the electrode metals (ideally) remain pure in composition. By contrast, most LMBs employ a single electroactive metal that migrates from the anode, through the salt, and alloys with the cathode during discharge. The Na-Zn cell owes its unusually high voltage to this departure from the 'classical' LMB design, however it also suffers disadvantages. Most important is self-discharge, which can occur if Zn^{2+} ions in the salt come into contact with the Na electrode, where they can be reduced to metallic Pb directly [10,11,15,25,26]. A porous ceramic membrane ('diaphragm') can be used to separate the upper and lower parts of the electrolyte to alleviate undesirable mass transfer between the electrodes [14,28], and thus to mitigate self-discharge. Al_2O_3 membranes have been used in the past due to their chemical and thermal stability properties [13].

The general requirement that any LMB's components all remain molten necessitates high operating temperatures, and values in excess of 200 °C are common [5,29,30]. These temperatures present design challenges such as enhanced cell-body corrosion, and safety concerns [21], but also confer performance advantages, since electrolyte resistance and kinetic barriers to electron-transfer are decreased. Lower temperature systems have been proposed [30], but these suffer disadvantages in terms of capacity and scalability. The Na-Zn cell requires one of the highest operating temperatures among LMBs: 557 °C at the minimum. This is because in addition to the need for its salt electrolyte to remain molten, Na-Zn operation depends on Na and Zn being immiscible, and not forming an alloy which cannot be separated into its pure components. This necessary immiscibility only prevails above 557 °C [13].

The identification of electrode and electrolyte materials for liquid metal batteries is critical for the design and operation of a LMB. In general, the main challenges are to find electrode materials that provide a favorable cell potential, while also remaining cost-effective. Different methodologies have been proposed to select them under different criteria [9], and several material options have been proposed in the past, such as Li-Bi, Pb-Sb, Ca-Bi [10–12] as examples. Recently, examples of systems where electrode alloying is promoted for better performance have also been proposed [27,31].

For anode materials, low-density, low melting temperature metals are preferred, thus Li has been a popular candidate for a number of designs [10,17], however, Lithium is expensive and not always easily available. Other options of anode material are suitable alternatives, as they are relatively cheap and safe. Other alternatives such as Gallium [18] or sodium-potassium alloy [19,20], have been proposed, in an effort to leverage their very low melting temperatures, but are not easily scaled to massive storage applications due to cost and safety concerns [20,21].

In contrast, suitable materials for the cathode are often prohibitively expensive, of low abundance [22], or have other unfavorable properties, such as promoting corrosion and other forms of cell degradation [5]. This leads to limited favorable options, but among these, Zn is particularly attractive due to its low cost and safety advantages [17].

Batteries based on the Na-Zn electrode pair have previously been proposed and appear to be a promising alternative [13–15]. This selection of materials has been motivated by their high abundance and low cost, while also providing an excellent cell potential, estimated at being approximately 1.8 V. With this material selection, an operating temperature of approximately 600 °C is necessary to maintain both the electrodes and the molten salt electrolyte in liquid state. This can lead to increased cost and a more complex design, but the low cost and availability of Zn over other cathode materials, and the availability of Na, makes this battery chemistry particularly attractive for large-scale stationary applications. In addition, electrolyte components that are compatible with this electrode combination are cheap and readily available, namely NaCl, $ZnCl_2$ and others [23,24].

There are numerous options of molten salts that can potentially be used in combination with Na-Zn cells. In principle, the molten salt is typically chosen as a mixture of the corresponding chlorides of

the electrode materials, with possibly other salts mixed in to alleviate problems of miscibility or corrosion. Addition for example of iodides, can significantly reduce the melting point, but comes with increased cost [5]. The melting point of the electrolyte must be compatible with the operating temperature of the electrodes and should exhibit a high ionic conductivity with a low electronic conductivity [2,5,25–27].

Ideally, a Na-Zn cell would have the capacity to store as much charge as there is Na salt in the electrolyte in its discharged state. Hence, this working principle could provide a theoretical upper limit of approximately 458 Ah per kg of initial NaCl, as an example. In practice however, the salt's melting temperature is sensitive to its chemical composition, and increases as the salt becomes more $ZnCl_2$-rich. Thus the true cell capacity is limited by the salt's tendency to freeze as its composition changes.

Previous studies have aimed to understand a multitude of physical phenomena associated with LMBs, such as solutal convective effects [32–34], and magneto-hydrodynamic effects, which also play a significant role in these cells, leading to electro-vortex flows and metal pad roll instabilities [35–37]. It has been mentioned that these hydrodynamic effects are very important for the large-scale operation of the cell as interfacial instability may add another design constraint when aiming to build larger batteries [38–42]. Understanding these convective phenomena is critical to avoid short circuits and improve the mass transfer properties of LMBs. Modeling of solute transport in the cathode of the cell has been done in the past [43,44]. In addition, ion transport in the electrolyte can also influence cell performance to a large extent, and this has been previously quantified for the case of Li-Bi cells [45] when fluid flow is neglected. This combination of physical and chemical processes makes comprehensive modeling of liquid metal batteries particularly challenging.

One must also take into account that during the cycling of the cell, there is a simultaneous dissolution and electro-deposition process in the electrode surface. Throughout the charge/discharge cycles, the composition of the electrolyte would be expected to change, and as such, the amount and initial composition of the salt would be linked to the overall capacity of the cell. With variation in composition, the conductivity of the electrolyte would also change. This compositional variation in the electrolyte dictates some of the operational limits of the cell, since this the one with the highest resistivity, and accounts for most of the Ohmic losses [44,46].

An outcome of the large contrast in density between the NaCl and $ZnCl_2$ salts is that the volume – and hence also the thickness – of the electrolyte changes during cycling. This leads to significant variation in the internal resistance of the cell, since this is the phase with the highest resistivity, accounting for most of the cell's Ohmic losses [44,46]. Electrolyte volume changes are however difficult to model accurately, and have therefore not yet been fully explored. Previous investigations have considered simplified systems, such as those with static interfaces, at several layer thicknesses [47].

Several previous studies have modeled transport processes in other aspects of liquid metal batteries [10,44]. In this study, we present a simplified unidimensional model that can consider most of the mass transfer effects contained in the interaction between the molten salt electrolyte and the electrodes of a Na-Zn cell. Our approach is similar to that of [45], but accounts for the variation in thickness of the different layers to determine the impact of these changes on the operation and performance of the cell. We approached this problem by developing a multiphase-flow method using a Volume-of-Fluid method for an arbitrary number of species, capable of handling both miscible and immiscible sets of phases [10,44]. To study exclusively the effects of migration and diffusion in detail, more complex convection effects are neglected by our model.

The main motivation of this model is to resolve the electrolyte volume change taking place as a result of the metal displacement reaction of the cell, while also resolving the species distribution within the electrolyte. With this information, we model the resulting changes in internal potential distribution and assess the mass transfer overpotential of the cell under different conditions.

The proposed method is compared against a simplified, small-scale experiments to verify the variation in voltage and current dependency.

2. Methodology

2.1. General model description

The model was conceived as a three-layer assembly, representing the electrodes and the electrolyte layer as shown in Fig. 1. The dimensions chosen allow for the Na layer to be thicker since it is of significantly lower density than the other materials, and thus an equivalent charge transfer would lead to a deeper erosion of the sodium layer than the Zn layer. The system is modeled in these dimensions such that it is reasonable to neglect hydrodynamic effects and focus on the mass transfer processes that can be resolved unidimensionally.

Initially, the electrolyte layer is modeled as a mixture of NaCl and $ZnCl_2$, thus considered as a mixture of three species: the Na^+, Cl^- and Zn^{2+} ions. For the respective ions, this corresponds to mole fractions of 0.583, 0.25 and 0.167 for Cl, Na and Zn. Although most available studies related to this battery chemistry also include other salts, such as $CaCl_2$, this configuration was selected because it contains minimal electrochemically relevant ions under idealized conditions, limiting the model to the observation of the ions that would react at the electrode surface. We later introduce $CaCl_2$ to the electrolyte for the purpose of experimental comparison.

Constant current J_0 and constant potential ψ_0 conditions were applied to the domain from the electrode boundaries in the longitudinal direction to observe the variation in concentration of the electrolyte components. The formation and dissolution of the electrode materials at the interfaces were simultaneously resolved, resulting in interface displacement. The current densities used were 100, 200, 500, 1000, 2000 and 5000 A/m^2 for constant current cases and voltage differences of 0.002, 0.004, 0.01, 0.02, 0.04, 0.1 V. These were repeated while inverting the sign of the current or voltage, to simulate the charge and discharge processes. In all tests, the temperature is assumed constant at 600 °C to justify the electrolyte remains in a liquid state, as reducing the temperature can lead to solidification, causing capacity loss and increased cell resistance.

2.2. Inclusion of $CaCl_2$ and experiment comparison

Addition of other salts is beneficial since it reduces the activity of Zn in the Na electrode, and thus leading to less self-discharge under real conditions. Therefore, at a second stage, $CaCl_2$ was added by including the Ca^{2+} ion and increasing the proportion of Cl^-.

For this second set of simulations we aimed to create a set of settings that would resemble the conditions of a small scale test cell that could be compared to experimental data. Simulations start in a discharged state with only a small amount of Na present initially. The current passes through the cell, leading to further sodium deposition that simulates the charge of the cell.

The resulting overpotential results were then compared with the experimental data obtained in a small-scale cell. In this way, the total variation of voltage after a given time was quantified and compared with an equivalent experimental setup.

Our first goal with the experimental comparison is to use the magnitude of the potential variation at a given time-scale to identify and measure the maximum internal current density of the cell. Since in the real cell the electrodes are of different dimensions, it is possible to measure only the total current externally, and thus understanding the magnitude of the internal current density can provide valuable information for future design improvement.

Since in real conditions, the system exhibits significant self-discharge at this scale, it was only possible to carry out an initial comparison during the charge process.

2.3. Experimental setup

To experimentally investigate the charging process, a simplified Na-Zn cell was constructed. The cell was assembled in the discharged state, initially containing a pool of liquid Zn of 5 mm thickness, beneath a 5 mm thick layer of molten salt (an equimolar mixture of NaCl and $CaCl_2$). A glassy carbon crucible served as both the cell body and the positive-electrode current collector. The negative-electrode current collector was a Ni coil, immersed into the salt to a depth of approximately 1 mm. The initial thickness of the molten salt layer is approximately 5 mm between the collector and the cathode. For simplicity, the porous diaphragm typical of Na-Zn cells was omitted. The cell was charged at a constant current of 100 mA using a potentiostat. The formation of Na during charging was demonstrated by a cell potential of 1.8 V, emission of dark vapors, and discoloration of the salt surrounding the negative electrode.

The surface area of the salt-Zn interface is constant value of approximately 10 cm^2 throughout the charging process. However, the calculation of this surface area is complicated by the wetting behavior of the Zn as it generally assumes a domed shape. In the first approximation, the surface area of the negative electrode is unknown due to the Ni coil's poorly defined geometry, and the changes in area caused by deposition of Na. We will the model described in this paper to determine the effective current density at the anode by observing the potential variation rate. A more complete description of the experiment is provided in the supplementary information.

2.4. Governing equations

The proposed model uses different equations for miscible and immiscible components. Three immiscible components are defined first, representing the two electrodes and a region containing the electrolyte mixture, and their volume fraction α_k is governed by Eq. (1) using the Volume-of-fluid method

$$\frac{\partial \alpha_k}{\partial t} = R_k, \tag{1}$$

where k is an index representing the sodium electrode, the zinc electrode, or the electrolyte layer. R_k is the reaction rate as a result of the current transfer at the interface. This term is calculated using Faraday's law as shown in Eq. (2)

$$R_k = \nabla \cdot \sum_{i \neq k} \frac{\alpha_k \mathbf{j} \delta_{k,i} \rho_k}{\eta_{k,i} N_A e_c M_k}, \tag{2}$$

where e_c is the elementary charge, N_A is the Avogadro number, $\eta_{k,i}$ is the number of electrons transferred per mol at the electrode-electrolyte interface against phase i and $\delta_{k,i}$ is an interface indicator function, defined as in Eq. (3), where α_i is the volume fraction of the phase α_k reacts with. $\mathbf{j}$ is the local current density at the electrode surface, defined as $\mathbf{j} = -\kappa \nabla \psi$, where κ is the local electric conductivity and ρ_k is the density contribution of each ion k.

$$\delta_{k,i} = \frac{\alpha_k \nabla \alpha_i - \alpha_i \nabla \alpha_k}{|\alpha_k \nabla \alpha_i - \alpha_i \nabla \alpha_k|} \tag{3}$$

The molar concentration of each of the immiscible components is retrieved by dividing it by the corresponding molar volume:

$$c_k = \frac{\alpha_k \rho_k}{M_k}. \tag{4}$$

Within the electrolyte layer, the Nernst–Planck equation governs the transport of each of the ionic components. The molar concentration of each ion species is given by Eq. (5):

$$\frac{\partial c_i}{\partial t} = -\nabla \cdot \mathbf{N}_i + R_k, \tag{5}$$

where the flux of i, $\mathbf{N}_i$ is given by the combination of diffusion, and migration, as shown in Eq. (6). The last term is the net reaction rate at the electrodes, defined as $R_k = \sum_k \frac{\partial c_k}{\partial t}$, where c_k is the molar concentration of the kth reacting component, thus the final term ensures that the molar reaction rate appearing in the electrolyte matches the reaction rate of the electrode surface,

$$\mathbf{N}_i = -D_i(\nabla c_i) - \frac{D_i e_c z_i}{k_B T} c_i \nabla \psi, \tag{6}$$

where D_i is the corresponding diffusion coefficient, z_i is the ion valency, k_B is the Boltzmann constant. ψ is the electric potential, given by Eq. (7), which ensures charge conservation in the conversion from ionic current to electronic current and vice versa as the charge crosses the interface between the electrolyte and the electrode.

Eq. (7) is obtained by adding the Nernst–Planck equation for each ionic species and converting each concentration into its equivalent charge density. In principle, the vicinity of the electrode should have a higher composition of the ion of opposite charge to the electrode surface, creating the electrical double layer [48], but since the double layer is much thinner than the thickness of the electrolyte, the system is assumed to be electroneutral, thus cancelling out the accumulation of charge, and resulting in Eq. (7) [45,49]. The electrical double layer can be assumed to be thin because the electrolyte layer is very thick by comparison, and molten salt electrolytes tend to have a high conductivity [50]

$$\nabla \cdot ((\kappa_e + \kappa_I) \nabla \psi) = -\nabla \cdot \sum_i N_A e_c z_i D_i \nabla c_i. \tag{7}$$

The quantities κ_e, are the volume fraction-averaged electronic conductivity, and κ_I is the ionic conductivity of the electrolyte. The right-hand side of the equation accounts for the net diffusion current [45]. The potential equation, defined in Eq. (7) uses the combination of the electronic conductivity κ_e and the ionic conductivity κ_I. The later is given by the approximation shown in Eq. (8). This equation is derived from the Nernst-Einstein approximation, which was originally derived for dilute electrolytes but has been used successfully to represent the dependence between concentration and conductivity of molten salts in the past [49]:

$$\kappa_I = \sum_i \frac{D_i e_c^2 N_A z_i^2}{k_B T} c_i \tag{8}$$

The mass density of the molten salt is calculated as a mole-fraction-weighted average of its local compositions, and the density contribution from each ion is obtained from a regression of the data found in literature [50], where the individual ion contribution to density has been determined to be as shown in Table 1. The electronic conductivity is calculated as Eq. (9):

$$\kappa_e = \sum_i \kappa_i \alpha_i. \tag{9}$$

Where in practice the electronic conductivity is only non-zero in the cells that are occupied by the electrode. With this approach, we aim to model the interface displacement process taking place when applying current through the given assembly of materials. Since we are primarily focused on observing the integrity of the interfaces and the evolution of the concentration profiles, we neglected all hydrodynamic effects, including buoyancy, for the purpose of this study. Furthermore, the charge transfer overpotential is assumed to be negligible, such that discontinuous potential distributions at the interface are not modeled [51]. This is justified as it is known that the liquid interfaces allow for almost unhindered charge transfer between the electrode and the electrolyte [10].

As a consequence of using Eq. (7) for modeling the potential, we assume that all electronic current approaching the interfaces causes a net ionic current of equal magnitude on the opposite side.

For the purposes of this work it is assumed that the phase change only takes place between the ion and its matching metal. Namely, Na^+ can only be released at the Na interface, and the Zn^{2+} ion can only be reduced at the Zn surface. Thus, no co-deposition is allowed, and the

Table 1
Physical properties of system components. The diffusion coefficients are approximated on the basis of their collective ionic conductivity, and the relative densities of the ions were adjusted to reflect the contributions of individual ions [50,52].

Component	ρ_i [$\frac{kg}{m^3}$]	M_i [$\frac{kg}{kmol}$]	D_i [$\frac{m^2}{s}$]	z_i	κ_e [$\frac{S}{m}$]
Na^+	1570.00	23	$6.82 \cdot 10^{-9}$	+1	–
Zn^{2+}	2580.00	65	$1.97 \cdot 10^{-9}$	+2	–
Cl^-	2470.00	35	$1.19 \cdot 10^{-9}$	−1	–
Ca^{2+}	2206.00	40	$1.69 \cdot 10^{-9}$	+2	–
Na	817.12	23	–	–	$3.471 \cdot 10^6$
Zn	6436.67	65	–	–	$2.739 \cdot 10^6$

values of the transfer coefficient η_{ij} are 1 for the $Na - Na^+$ reaction and 2 for the $Zn - Zn^{2+}$ reaction. The reaction term is not added when the components in question are not reactive, which in this case corresponds to the Cl^- ion.

2.5. Numerical model

These equations were implemented using the formulation of the finite volume method based on OpenFOAM. The model is based on the OpenFOAM solver *multiphaseInterFoam* [53], which was modified to accept the solution of miscible species within the electrolyte layer, as well as interfacial phase exchange, following the magnitude of the current passing through the system in accordance to Faraday's law.

The computational domain is discretized unidimensionally and in only the direction normal to the electrode surfaces. We discretized the domain in 1000 cells of equal size. This grid resolution was considered sufficient to capture concentration gradients, and grid dependency studies are provided as supplementary information. Time derivatives are discretized using the first-order Euler scheme, the divergence operators in Eq. (6) are discretized using the second-order upwind scheme, while the Laplacian term in Eq. (7) was discretized using second-order central differences.

These equations controlling the evolution of the immiscible layers are solved explicitly, while the species distribution within the electrolyte phase is solved implicitly.

3. Results and discussion

As an initial example of the discharge process, it is possible to visualize the enrichment of the electrolyte in sodium ions while the existing zinc is deposited in the bottom layer in Figure A.5, showing the evolution of the composition until it reaches its fully discharged state.

It can be noticed that the total electrolyte layer thickness increases during discharge due to the difference in density between the initial condition and the discharged state. This is also possible because the molar volume of sodium is much lower than that of zinc, and thus for a given current, the sodium interface advance is significantly higher, as shown in Eq. (2).

The resulting species distributions after charge and discharge under high and low current conditions are shown in Fig. 2 as stacked area plots. Here, one can visualize the proportion of each component occupying space, noticing the sodium and zinc electrode regions on the side and the overlapped areas showing the electrolyte components.

The initial state of the simulations is shown in the upper half of Fig. 2, showing the mole fraction at the initial state. After submitting this composition to charge or discharge, the distributions obtained are shown in the bottom half of Fig. 2. The simulation ended when the depositing electrode lost contact with its corresponding reacting ion. So during discharge, the simulations are ended when the Zn^{2+} concentration drops to zero near the zinc interface.

It can be observed in the final distributions that the final states at high and low currents are different, as the species distribution in the electrolyte layer is linked with the magnitude of the migration flux, so at higher currents, stronger concentration gradients are observed, limiting the amount of charge that can be stored or extracted from the cell.

In the high current example shown in Fig. 2, one can observe a nonmonotonic mole fraction distribution in the remaining Zn^{2+} after discharge. This is due to the combined effect of the reaction rate near the depositing interface and the displacement of Zn^{2+} created from the release of Na^+ on the Na surface. At lower current densities, the magnitude of these concentration gradients is much lower, ensuring a deeper depth of discharge as it takes longer for the electrode to deplete the available reacting ion.

The potential distribution at initial and final conditions for each case is shown in Fig. 3(a). In all cases it is shown that the variation of the thickness in the electrolyte layer creates a modification of the potential field, resulting in increased total resistance as the layer becomes thicker, and the opposite when it shrinks. In the constant current cases, the potentials are adjusted while maintaining an equivalent current through the cell; however, because the conductivity of the cell is also changing, the slope in the potential field also changes.

The constant potential cases show that the difference in current is mostly perceived in the electrolyte layer, as the electrodes have significantly higher conductivity, and thus the variation in current is directly linked to the expansion of the electrolyte layer. The lower current and applied voltage cases show a larger change between the initial and final configurations due to the more stable charge/discharge process.

A closer look at the potential distribution in the electrolyte can be seen in Fig. 3(b), where the shift in the distribution due to the thickness change can clearly be seen. Additionally, it is possible to see that the deeper discharge possible in the low-current/low-voltage cases results in greater variations in this shift between the initial and final states.

The charge capacity stored or released by the system was calculated by integrating the current density through the anode boundary in time as shown in Eq. (10). And the capacity change over time is displayed in Fig. 4 for all cases. Here it is possible to see how the cell can be charged to a higher capacity by limiting the charging current

$$C = \int \mathbf{j} \cdot \hat{\mathbf{n}} dt, \tag{10}$$

where C is the capacity of the cell, and $\hat{\mathbf{n}}$ is the unit surface-normal vector at the boundary of the system.

The maximum capacity per unit area of the cell is calculated as in Eq. (11)

$$C_{max,i} = z_i F c_{0,i} \Delta x \tag{11}$$

where component i corresponds to the depositing ion, $c_{0,i}$ is its initial molar concentration and Δx is the initial thickness of the electrolyte layer. Under charge operation, this corresponds to Na^+, and in discharge mode, this corresponds to Zn^{2+}. Under the current initial conditions, the maximum capacity of the cell under discharge mode is therefore approximately 2128 Ah/m^2 and 1829 Ah/m^2 for charge mode.

The relation between the maximum capacity and the discharge time may appear to have a discrepancy with the amount of charge that should theoretically have passed through the cell. This can be explained by the combined contribution of the diffusion current and the amount

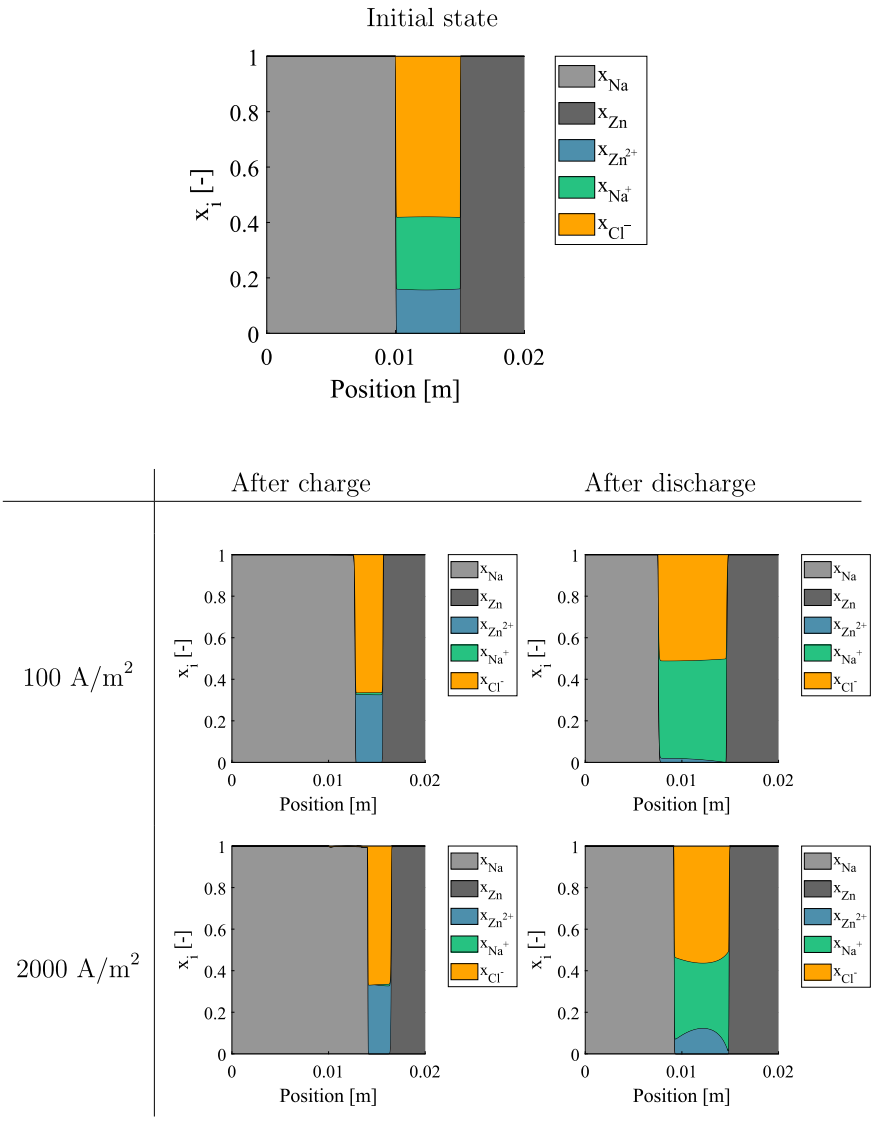

Fig. 2. Area plot of the battery components (presented horizontally) in the initial state of the simulation. The Left side contains the sodium electrode and the right side the zinc electrode. The stacked areas represent the mole fraction of each ion in the electrolyte (top). Final states at two different current densities are shown below after charge and discharge.

of current that remains in the cell after it has reached its mass transfer limit.

During discharge, the cell appears to behave similarly regardless of whether it is discharged under constant current or constant potential conditions, as it reaches similar discharge limits.

The maximum usable capacity for each case is shown in Fig. 5 , where the impact in capacity loss as a result of fast cycling can be clearly observed. In our production, the effect during discharge seems to be somewhat more pronounced.

In Fig. 6 the corresponding cell potential difference achieved under constant current conditions are shown in the left column, while the right column shows the cell current variation under constant potential. The constant current cases show a smooth decline in the potential during charge, showing the thinning of the electrolyte layer is the dominant factor. When charging the cell under constant potential, predictably the cell current increases as the total cell resistance is lower. Under discharge, the potential does not appear to change much under constant current, presumably because of the electrolyte thickness increase offsetting the effect of the diffusion current, since it has been observed that electrolyte thickness has large impact on cell potential [47]. Under constant potential discharge, however, the current seems to vary non-monotonically with a small initial increase and then a decrease over time. This may also be an effect of the initial separation of the components, causing an anisotropic conductivity in the electrolyte layer, and then being offset by the increased resistance associated with the electrolyte expansion.

From these observations, we can speculate that the interplay between the diffusion current and the volumetric changes in the cell may be an important aspect when defining the operation limits and cell size of a sodium-zinc liquid metal battery. Significant differences in usable capacity can be determined by the interaction between these variables, and therefore, it should be considered when determining the optimal size and operation range of a battery design.

It must be noted that these observations are caused by the compositional variation within the cell, but this would only suggest that these effects may be very important depending on the dimensions of the cell. The accumulation of Zn ions near the Na electrode, leading to parasitic discharge, highlights the importance of the introduction of a diffusion barrier to mitigate this effect, such as the one introduced by Xu et al. [14], however, one must consider that this appears in these results in the absence of convective effects, and thus additional mixing would mitigate this to some extent.

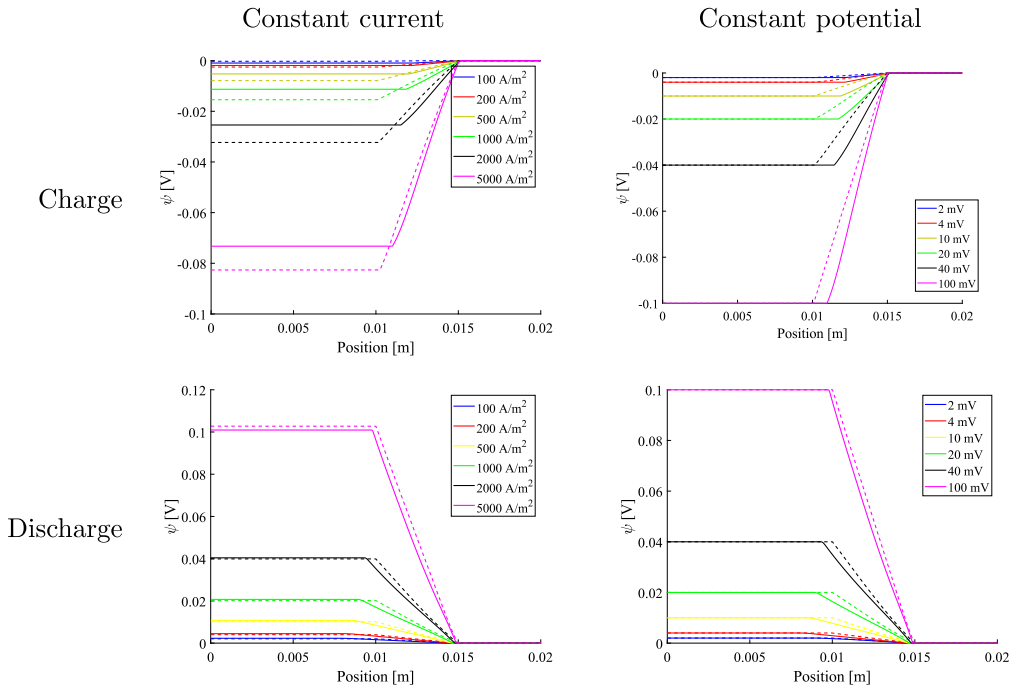

(a) Whole system

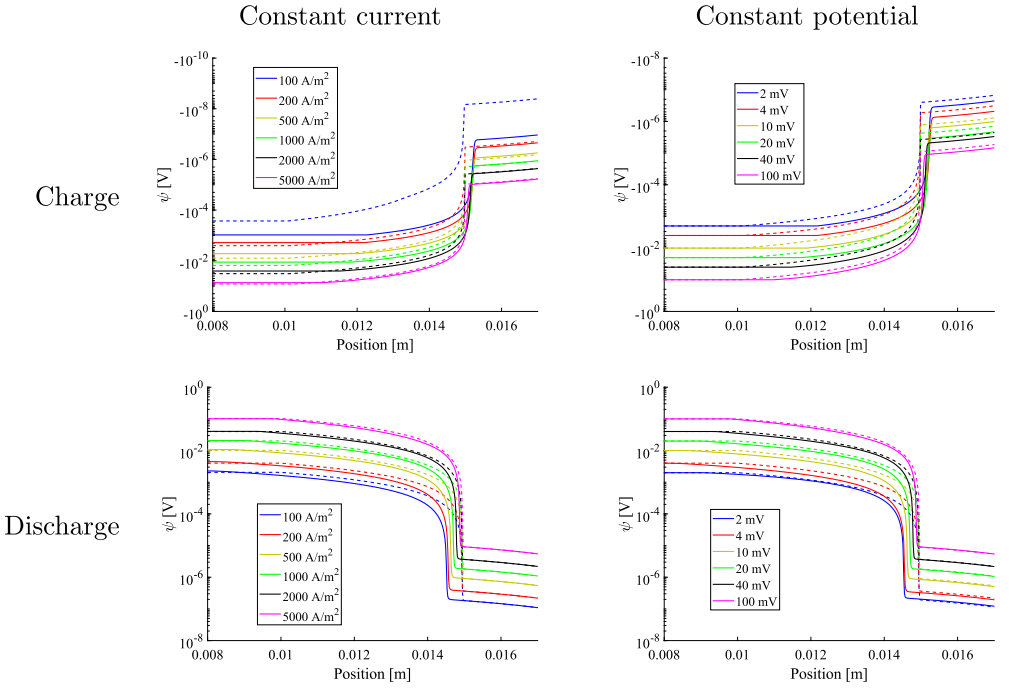

(b) Within electrolyte

Fig. 3. Potential distributions across the cells (oriented horizontally). The dashed line is the initial state and the solid line is the final configuration. The distribution across the whole system is shown in part (a) while the corresponding distribution within the electrolyte is shown zoomed in (b).

3.1. Experimental comparison

As a preliminary assessment of the performance of our model, we compared the voltage variation during the simulated charging process with the experiment described in Section 2.3. In the experiment, the cell potential increases until it reaches a limit after around 300 s. We compared this observed change in voltage with the overpotentials predicted by our model, using the final experimental voltage (attained after 300s) as a reference. The simulation was run using the same dimensions as in the experiment. In the simulation we performed a parameter sweep, modeling different current densities, to see which most closely reproduced our experimental data. This was done to illustrate the first-order consistency between the internal performance parameters of the experimental cell and the simplified model. In essence, by matching the magnitude of the overpotential variation during charge, we used our model to estimate the current density at the Na electrode.

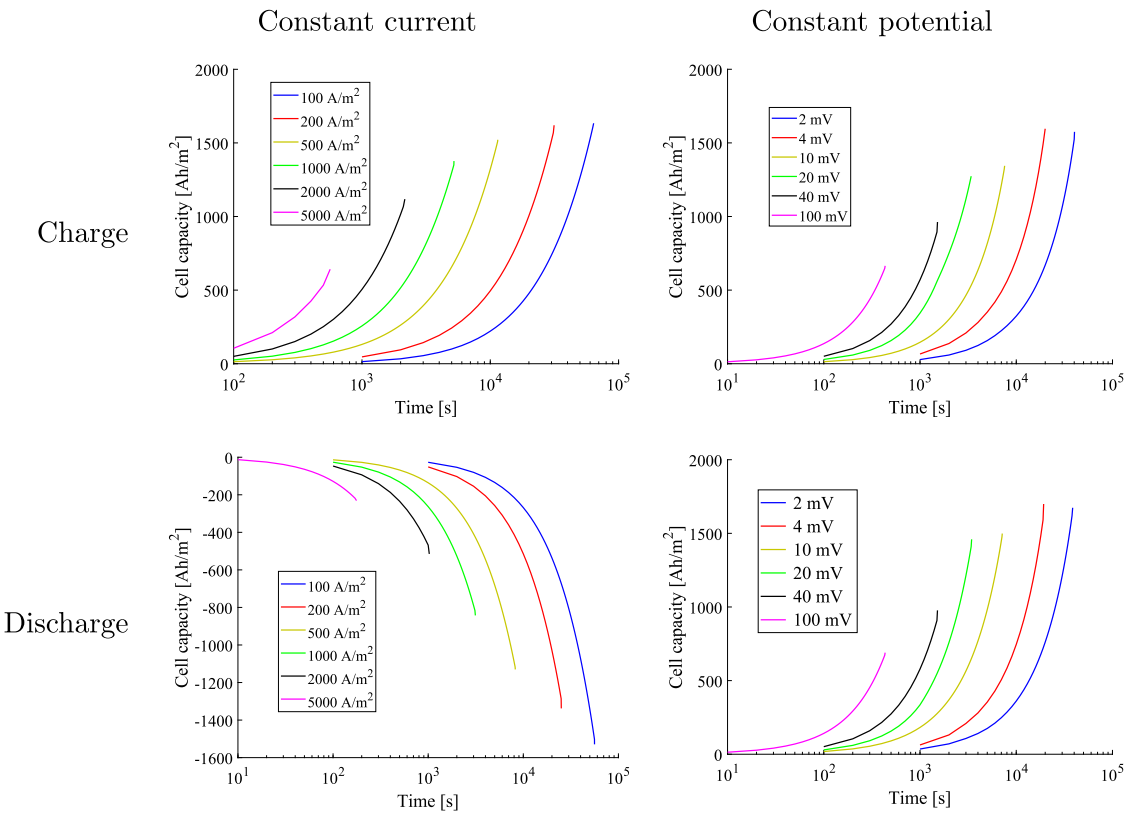

Fig. 4. Cell capacity over time for each case.

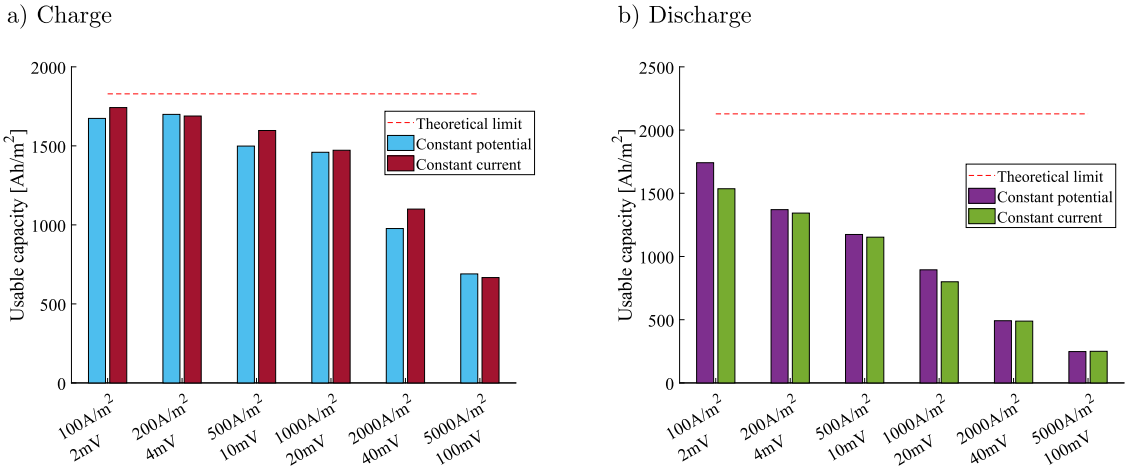

Fig. 5. Chart of usable capacity for each case under charge (a) and discharge (b), the maximum theoretical capacity that could be charged or discharged is shown in red dashes. (For interpretation of the references to color in this figure legend, the reader is referred to the web version of this article.)

Fig. 7(a) shows the simulated change in overpotential magnitude during the charging process for different current densities (solid lines), compared to the experimentally observed voltage variation (red dashed line), obtained by passing a current of 100 mA through the cell. Since we are plotting the difference between the voltage at any instant and the final 'steady state' voltage attained after 300 s, the displayed value declines to zero (this zero point corresponding to the plateau at a specific value: 1.8 V in the experiment). Of all the charge densities modeled, the experimental data most closely fit the 4000 A/m^2 case. Combining this best-fit value with the known experimental current (100 mA/cm^2), we can estimate the surface area of the Na electrode as 25 mm^2. While we were unable to measure the surface area of the Na pool directly, its surrounding Ni coil had an outer diameter of 5 mm, which will have limited its cross-sectional area to approximately 20 mm^2. Thus, the current density predicted by the model on the basis of matching the observed overpotential change is broadly consistent with the results from our experimental cell. It should be noted however that since the model neglects transport by advection, the overpotentials it predicts are likely to be over-estimates. Thus its predicted current density should be considered a lower limit, and hence an upper limit on the surface area of the Na electrode in our experiment. This, too is consistent with the configuration of our cell, since the Ni coil constrains the electrode area, as previously indicated, to be no larger than a value of approximately 20 mm^2.

Although it is difficult to measure discharge under the same conditions due to the action of self discharge mechanisms not covered by

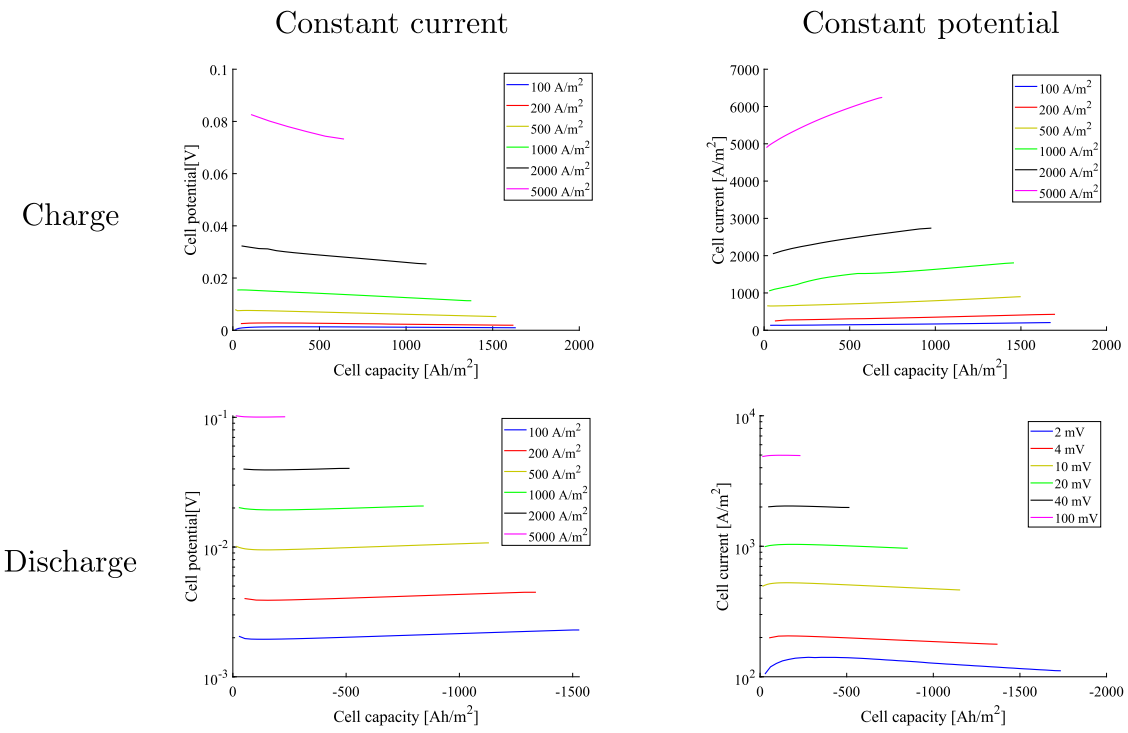

Fig. 6. Cell current and cell voltage for each case against capacity.

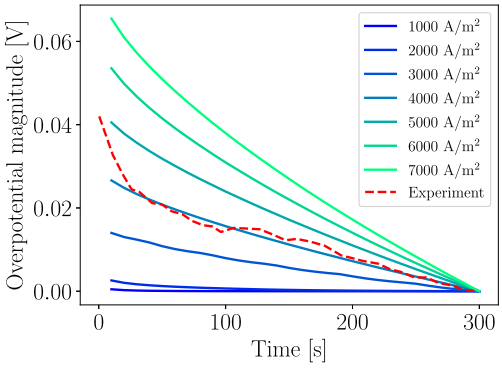

(a) Experiment comparison

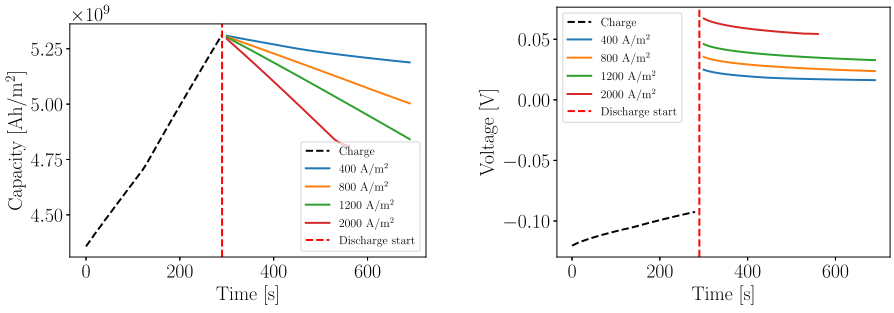

(b) Cycling simulation

Fig. 7. (a) Comparison of the total overpotential variation magnitude during charge at different current densities compared with experiment at 100 mA in charge. The values are presented based on the reference potential of 0 V at the end of the charge at 300 s. (b) Capacity and voltage variation n a cycle with 300 s of charge at 4000 A/m^2, followed by 400 s of discharge at different current densities.

this model, we can carry out a performance test by charging the cell at the current density identified, and then discharging it at 400, 800, 1200 and 2000 A/m^2. The potential variation and the capacity change in these conditions are shown in Fig. 7(b).

The capacity steadily increases during the first 300 s of charge, while the cell voltage decreases due to the electrolyte layer getting narrower. After this, the cell is discharged at different current densities, and it is possible to observe a drop in the measured cell potential that is proportional to the current density used for the discharge. It can be noticed that at high discharge rate, the capacity of the cell is cut short due to the concentration gradients created during charge.

4. Conclusions

Using a simplified multiphase approach, it was possible to model the volumetric changes taking place as a result of the charge and discharge of a Na-Zn liquid metal battery. Significant changes in volume are observed due to the relatively low density of sodium compared to the molten salt electrolyte leading to significant variation in the electrolyte thickness and therefore in the potential distribution across the cell.

It was shown that concentration gradients in the molten salt composition can lead to the depletion of the reacting ions near the electrode surface and therefore operation limits must consider these concentration gradients. It was possible to show how a simplified 1D model can be used to understand internal current distribution based on potential variation.

The importance of this electrolyte compositional variation has been highlighted before, but its impact joined with the volumetric changes in the electrolyte leads to a more complex phenomenon that can potentially have significant impacts on cell performance.

This behavior might be partially mitigated by other transport phenomena that have been neglected in the present work, such as compositional convection and convective effects, or magnetohydrodynamic effects.

Future work will address the linkage between chemical composition variation and hydrodynamic effects. The introduction of separator membranes and its impact on species distribution in the electrolyte is also an important factor that should be studied.

Given that this simplified model does not include comprehensive modeling of the open cell voltage, including this in future work would enable more comprehensive comparison with experimental results. Subsequently, additional phenomena that cannot be resolved unidimensionally should also be considered. Especially the effect of having nonplanar electrode-electrolyte interfaces and other electrocapillary phenomena, given the high interfacial tension between these materials.

Declaration of competing interest

The authors declare that they have no known competing financial interests or personal relationships that could have appeared to influence the work reported in this paper.

Data availability

Data will be made available on request.

Acknowledgments

This project received funding from the European Union's Horizon 2020 research and innovation programme under grant agreement No. 963599. All authors approved the version of the manuscript to be published.

Appendix A. Supplementary data

Supplementary material related to this article can be found online at https://doi.org/10.1016/j.est.2023.109147.

References

[1] S. Zhang, Y. Liu, Q. Fan, C. Zhang, T. Zhou, K. Kalantar-Zadeh, Z. Guo, Liquid metal batteries for future energy storage, Energy Environ. Sci. (2021) http://dx.doi.org/10.1039/d1ee00531f.

[2] T. Weier, A. Bund, W. El-Mofid, G.M. Horstmann, C.-C. Lalau, S. Landgraf, M. Nimtz, M. Starace, F. Stefani, N. Weber, Liquid metal batteries - materials selection and fluid dynamics, in: IOP Conference Series: Materials Science and Engineering, Vol. 228, IOP Publishing, 2017, 012013, http://dx.doi.org/10.1088/1757-899X/228/1/012013.

[3] I. Hadjipaschalis, A. Poullikkas, V. Efthimiou, Overview of current and future energy storage technologies for electric power applications, Renew. Sustain. Energy Rev. 13 (6–7) (2009) 1513–1522.

[4] A. Solheim, K.S. Osen, C. Sommerseth, O.E. Kongstein, Liquid metal batteries as a power buffer in aluminium production plants, (2016), 2017, pp. 2–5.

[5] H. Kim, D.A. Boysen, J.M. Newhouse, B.L. Spatocco, B. Chung, P.J. Burke, D.J. Bradwell, K. Jiang, A.A. Tomaszowska, K. Wang, W. Wei, L.A. Ortiz, S.A. Barriga, S.M. Poizeau, D.R. Sadoway, Liquid metal batteries: Past, present, and future, Chem. Rev. 113 (3) (2013) 2075–2099, http://dx.doi.org/10.1021/cr300205k.

[6] H. Li, H. Yin, K. Wang, S. Cheng, K. Jiang, D.R. Sadoway, Liquid metal electrodes for energy storage batteries, Adv. Energy Mater. 6 (14) (2016) 1600483, http://dx.doi.org/10.1002/aenm.201600483, _eprint: https://onlinelibrary.wiley.com/doi/pdf/10.1002/aenm.201600483.

[7] W. Herreman, S. Bénard, C. Nore, P. Personnettaz, L. Cappanera, J.-L. Guermond, Solutal buoyancy and electrovortex flow in liquid metal batteries, Phys. Rev. Fluids 5 (7) (2020) 074501.

[8] P. Personnettaz, P. Beckstein, S. Landgraf, T. Köllner, M. Nimtz, N. Weber, T. Weier, Thermally driven convection in Li|| Bi liquid metal batteries, J. Power Sources 401 (2018) 362–374.

[9] H. Zhou, B. Li, M. Yu, S. Li, G. Fan, X. Ning, Accelerated design of electrodes for liquid metal battery by machine learning, Energy Storage Mater. 56 (2023) 205–217.

[10] J.M. Newhouse, Modeling the operating voltage of liquid metal battery cells by, 2014.

[11] X. Ning, S. Phadke, B. Chung, H. Yin, P. Burke, D.R. Sadoway, Self-healing Li-Bi liquid metal battery for grid-scale energy storage, J. Power Sources 275 (2015) 370–376, http://dx.doi.org/10.1016/j.jpowsour.2014.10.173.

[12] H. Kim, D.A. Boysen, T. Ouchi, D.R. Sadoway, Calcium–bismuth electrodes for large-scale energy storage (liquid metal batteries), J. Power Sources 241 (2013) 239–248, http://dx.doi.org/10.1016/j.jpowsour.2013.04.052.

[13] J. Xu, O.S. Kjos, K.S. Osen, A.M. Martinez, O.E. Kongstein, G.M. Haarberg, Na-Zn liquid metal battery, J. Power Sources 332 (2016) 274–280, http://dx.doi.org/10.1016/j.jpowsour.2016.09.125, Publisher: Elsevier B.V.

[14] J. Xu, A.M. Martinez, K.S. Osen, O.S. Kjos, O.E. Kongstein, G.M. Haarberg, Electrode behaviors of Na-Zn liquid metal battery, J. Electrochem. Soc. 164 (12) (2017) A2335–A2340, http://dx.doi.org/10.1149/2.0591712jes.

[15] F. Zhang, J. Jin, J. Xu, Z. Shi, Anode reaction mechanisms of Na|NaCl-CaCl2|Zn liquid metal battery, J. Energy Chem. 72 (2022) 81–87, http://dx.doi.org/10.1016/j.jechem.2022.04.035.

[16] W. Hamer, M. Malmberg, B. Rubin, Theoretical electromotive forces for cells containing a single solid or molten chloride electrolyte, J. Electrochem. Soc. 103 (1956) 8–16.

[17] S. Yan, L. Fan, H. Li, X. Zhou, H. Zhou, W. Zhang, Z. Li, Y. He, B. Li, K. Jiang, et al., Novel high-voltage Zn-based electrode based on displacement reaction for liquid metal batteries, ACS Sustain. Chem. Eng. (2023).

[18] H. Xie, H. Zhao, J. Wang, P. Chu, Z. Yang, C. Han, Y. Zhang, High-performance bismuth-gallium positive electrode for liquid metal battery, J. Power Sources 472 (2020) 228634.

[19] Y. Ding, X. Guo, Y. Qian, L. Xue, A. Dolocan, G. Yu, Room-temperature all-liquid-metal batteries based on fusible alloys with regulated interfacial chemistry and wetting, Adv. Mater. 32 (30) (2020) 2002577.

[20] Z. Tai, Y. Li, Y. Liu, L. Zhao, Y. Ding, Z. Lu, Z. Peng, L. Meng, G. Yu, L. Liu, Novel quasi-liquid K-Na alloy as a promising dendrite-free anode for rechargeable potassium metal batteries, Adv. Sci. 8 (16) (2021) 2101866.

[21] S. Wu, X. Zhang, R. Wang, T. Li, Progress and perspectives of liquid metal battery, Energy Storage Mater. (2023).

[22] D. Entr, Report on Critical Raw Materials for the EU, European Commission, Brussels, Belgium, 2014.

[23] H. Sun, G. Zhu, X. Xu, M. Liao, Y.Y. Li, M. Angell, M. Gu, Y. Zhu, W.H. Hung, J. Li, Y. Kuang, Y. Meng, M.C. Lin, H. Peng, H. Dai, A safe and non-flammable sodium metal battery based on an ionic liquid electrolyte, Nature Commun. 10 (1) (2019) http://dx.doi.org/10.1038/s41467-019-11102-2, Publisher: Nature Publishing Group.

[24] Q. Gong, W. Ding, A. Bonk, H. Li, K. Wang, A. Jianu, A. Weisenburger, A. Bund, T. Bauer, Molten iodide salt electrolyte for low-temperature low-cost sodium-based liquid metal battery, J. Power Sources 475 (2020) http://dx.doi.org/10.1016/j.jpowsour.2020.228674.

[25] H. Liu, X. Zhang, S. He, D. He, Y. Shang, H. Yu, Molten salts for rechargeable batteries, Mater. Today (2022) http://dx.doi.org/10.1016/j.mattod.2022.09.005.

[26] H. Zhou, H. Li, Q. Gong, S. Yan, X. Zhou, S. Liang, W. Ding, Y. He, K. Jiang, K. Wang, A sodium liquid metal battery based on the multi-cationic electrolyte for grid energy storage, Energy Storage Mater. 50 (2022) 572–579, http://dx.doi.org/10.1016/j.ensm.2022.05.032.

[27] W. Ding, Q. Gong, S. Liang, R. Hoffmann, H. Zhou, H. Li, K. Wang, T. Zhang, A. Weisenburger, G. Müller, et al., Multi-cationic molten salt electrolyte of high-performance sodium liquid metal battery for grid storage, J. Power Sources 553 (2023) 232254.

[28] H. Yin, B. Chung, F. Chen, T. Ouchi, J. Zhao, N. Tanaka, D.R. Sadoway, Faradaically selective membrane for liquid metal displacement batteries, Nature Energy 3 (2) (2018) 127–131, http://dx.doi.org/10.1038/s41560-017-0072-1, Publisher: Nature Publishing Group.

[29] D. Bradwell, D.A. Boysen, L. Ortiz, D.R. Sadoway, Liquid Metal Battery: An Electrometallurgical Approach to Large-Scale Energy Storage, No. 4, IOP Publishing, 2010, p. 187.

[30] Y. Ding, X. Guo, Y. Qian, L. Xue, A. Dolocan, G. Yu, Room-temperature all-liquid-metal batteries based on fusible alloys with regulated interfacial chemistry and wetting, Adv. Mater. 32 (30) (2020) 2002577, http://dx.doi.org/10.1002/adma.202002577, _eprint: https://onlinelibrary.wiley.com/doi/pdf/10.1002/adma.202002577.

[31] Y. Zhou, G. Li, B. Li, X. Ning, Operando formation of multi-channel positive electrode achieved via tellurium alloying in liquid metal battery, Energy Storage Mater. 53 (2022) 927–936.

[32] W. Herreman, S. Bénard, C. Nore, P. Personnettaz, L. Cappanera, J.-L. Guermond, Solutal buoyancy and electrovortex flow in liquid metal batteries, Phys. Rev. Fluids 5 (7) (2020) 074501, http://dx.doi.org/10.1103/PhysRevFluids.5.074501, Publisher: American Physical Society.

[33] P. Personnettaz, S. Landgraf, M. Nimtz, N. Weber, T. Weier, Mass transport induced asymmetry in charge/discharge behavior of liquid metal batteries, Electrochem. Commun. 105 (2019) 106496, http://dx.doi.org/10.1016/j.elecom.2019.106496.

[34] P. Personnettaz, S. Landgraf, M. Nimtz, N. Weber, T. Weier, Effects of current distribution on mass transport in the positive electrode of a liquid metal battery, 2021, arXiv preprint arXiv:2104.00144.

[35] O. Zikanov, Metal pad instabilities in liquid metal batteries, Phys. Rev. E 92 (6) (2015) 063021, http://dx.doi.org/10.1103/PhysRevE.92.063021, Publisher: American Physical Society.

[36] W. Herreman, C. Nore, P. Ziebell Ramos, L. Cappanera, J.-L. Guermond, N. Weber, Numerical simulation of electrovortex flows in cylindrical fluid layers and liquid metal batteries, Phys. Rev. Fluids 4 (11) (2019) 113702, http://dx.doi.org/10.1103/PhysRevFluids.4.113702, Publisher: American Physical Society.

[37] F. Stefani, V. Galindo, C. Kasprzyk, S. Landgraf, M. Seilmayer, M. Starace, N. Weber, T. Weier, Magnetohydrodynamic effects in liquid metal batteries, in: IOP Conference Series: Materials Science and Engineering, Vol. 143, IOP Publishing, 2016, 012024, http://dx.doi.org/10.1088/1757-899X/143/1/012024.

[38] W. Herreman, C. Nore, L. Cappanera, J.L. Guermond, Tayler instability in liquid metal columns and liquid metal batteries, J. Fluid Mech. 771 (2015) 79–114, http://dx.doi.org/10.1017/jfm.2015.159.

[39] D.H. Kelley, T. Weier, Fluid mechanics of liquid metal batteries, Appl. Mech. Rev. 70 (2) (2018) http://dx.doi.org/10.1115/1.4038699.

[40] G.M. Horstmann, N. Weber, T. Weier, Coupling and stability of interfacial waves in liquid metal batteries, J. Fluid Mech. 845 (2018) 1–35, http://dx.doi.org/10.1017/jfm.2018.223, Publisher: Cambridge University Press.

[41] S. Bénard, N. Weber, G.M. Horstmann, S. Landgraf, T. Weier, Anode-metal drop formation and detachment mechanisms in liquid metal batteries, J. Power Sources 510 (2021) 230339, http://dx.doi.org/10.1016/j.jpowsour.2021.230339.

[42] N. Weber, V. Galindo, F. Stefani, T. Weier, T. Wondrak, Numerical simulation of the tayler instability in liquid metals, New J. Phys. 15 (4) (2013) 043034.

[43] N. Weber, M. Nimtz, P. Personnettaz, T. Weier, D. Sadoway, Numerical simulation of mass transfer enhancement in liquid metal batteries by means of electro-vortex flow, J. Power Sources Adv. 1 (2020) 100004, http://dx.doi.org/10.1016/j.powera.2020.100004.

[44] N. Weber, C. Duczek, G.M. Horstmann, S. Landgraf, M. Nimtz, P. Personnettaz, T. Weier, D.R. Sadoway, Cell voltage model for Li-Bi liquid metal batteries, Appl. Energy 309 (2022) 118331, http://dx.doi.org/10.1016/j.apenergy.2021.118331.

[45] C. Duczek, N. Weber, O.E. Godinez-Brizuela, T. Weier, Simulation of potential and species distribution in a Li||Bi liquid metal battery using coupled meshes, Electrochim. Acta 437 (2023) 141413.

[46] D. Swinkels, Molten salt batteries and fuel cells, Adv. Molten Salt Chem. 1 (1971) 165–223.

[47] Y. Jiang, T. Cao, P. Song, D. Zhang, Y. Shi, N. Cai, Effects of magnetically induced flow on electrochemical reacting processes in a liquid metal battery, J. Power Sources 438 (2019) 226926.

[48] A.J. Bard, L.R. Faulkner, H.S. White, Electrochemical Methods: Fundamentals and Applications, John Wiley & Sons, 2022.

[49] J. Newman, N.P. Balsara, Electrochemical Systems, John Wiley & Sons, 2021.

[50] G.J. Janz, R. Tomkins, C. Allen, J. Downey Jr., G. Garner, U. Krebs, S.K. Singer, Molten salts: volume 4, part 2, chlorides and mixtures—electrical conductance, density, viscosity, and surface tension data, J. Phys. Chem. Ref. Data 4 (4) (1975) 871–1178.

[51] N. Weber, S. Landgraf, K. Mushtaq, M. Nimtz, P. Personnettaz, T. Weier, J. Zhao, D. Sadoway, Modeling discontinuous potential distributions using the finite volume method, and application to liquid metal batteries, Electrochim. Acta 318 (2019) 857–864.

[52] V. Sobolev, Database of thermophysical properties of liquid metal coolants for GEN-IV, 2011.

[53] C. Greenshields, H. Weller, Notes on Computational Fluid Dynamics: General Principles, CFD Direct Ltd, Reading, UK, 2022.